RSC Advances

PAPER

View Article Online
View Journal | View Issue

Cite this: *RSC Adv.*, 2021, **11**, 12771

Intelligent phase-transition MnO_2 single-crystal shell enabling a high-capacity Li-rich layered cathode in Li-ion batteries†

Deyuan Liu, Jian Yang, Junming Hou, Jiaxuan Liao and Mengqiang Wu *

Received 26th February 2021
Accepted 26th March 2021

DOI: 10.1039/d1ra01561c

rsc.li/rsc-advances

Layered, Li-rich Mn-based oxides (LLMOs) are the most promising next-generation, high-energy batteries due to their relatively high specific capacities and high voltages. However, the practical application of LLMO cathodes is limited by low initial coulombic efficiencies (CEs) and poor cycling performance. Herein, we used the reaction of $KMnO_4$ and $MnSO_4$ under hydrothermal conditions to grow a nano-SCMO shell on the LLMO material surface (SCMO@LLMO). The unique particle/sheet compound structure of the SCMO shell is beneficial to the electrochemical reaction. SCMO has good Li storage characteristics and excellent surface structure stability in the single-crystal phase which further improves the reversible capacity, CE, and cyclic stability of the LLMO cathode. Therefore, the optimal coated sample (feedstock: 2 M $KMnO_4$, SCMO@LLMO-2.0) exhibits a good initial discharge capacity (238.2 mA h g^{-1} at 1C and 173.8 mA h g^{-1} at 5C), initial CE (89.6% at 1C and 86.5% at 5C), and cycling performance (capacity retention of 84.67% at 1C and 62.72% at 5C after 200 cycles). This work adopts a hydrothermal method to synthesize a nano-single crystal composite material, laying a foundation for the preparation of the SCMO@LLMO cathodes for LLMO primary battery cathodes with high electrochemical performance.

1. Introduction

The increased demand for electric vehicles (EVs) has necessitated improvements in high energy density in Li-ion batteries (LIBs).[1,2] The cathode material is the key variable for increasing the energy density of LIBs.[3,4] However, high-nickel ternary cathode materials have pronounced capacity fading, especially at high voltages, leading to a limited cycle life.[5] Olivine-type $LiFePO_4$ exhibits limited rate capability due to its low ionic diffusivity and poor electronic conductivity.[6] Compared with traditional cathode materials, LLMO has a higher specific capacity (≥250 mA h g^{-1}) and high voltage (>4.5 V),[7–9] which is one of the research hotspots in the field of LIBs. However, the LLMO cathodes undergo irreversible cation and anion loss in the charging and discharging process, resulting in degraded performance characteristics such as a low initial CE,[10] poor rate performance,[11] and poor cycling stability.[12]

Extensive efforts have been made to inhibit cation/anion loss. Surface modification,[13–16] body phase doping,[17–20] and gradient treatment[21,22] have been successfully used for this purpose because the irreversible loss of oxygen mainly occurs on the material surface.[23,24] Surface modification can greatly improve the stability and dynamic performance of surface oxygen[25] which enhances the specific capacity and regulates the cycling stability of materials.[26,27] Currently, oxides,[28] platinum-group metals,[29] and low-dimensional carbon materials[30] are widely used in the surface coating of LLMO cathodes. However, the above coating methods only improve the performance of a certain aspect of the LLMO (such as reversible capacity), and a coating strategy to comprehensively improve electrochemical performance remains to be determined. In addition, compared with innovations in the compositions of coating materials, coating materials constructed by varying the grain orientation are rarely reported.

Single-crystal material is a kind of new material which is used more and more widely. It is composed of a single crystal whose diffraction pattern is a regular lattice. Single-crystal cathodes provide a new research direction for LIBs due to their high compressive strength and good machinability.[31] The single-crystal bulk phase improves the discharging voltage,[32] vibrational density,[33] and cycling performance[34,35] of LIBs. However, the larger particles (3–6 μm) of the single-crystal materials inhibit the diffusion of Li^+, resulting in poor initial CE, reversible capacity, and rate performance.[36] However, by selecting compounds with good electrochemical activities,[37] it is possible to improve the intrinsic properties of LLMO cathode materials. In this work, single-crystal compound shells with smaller particle sizes (≤50 nm) and good Li^+ insertion/extraction characteristics were synthesized *in situ* on the cathode material surface, providing a new fabrication scheme

School of Materials and Energy, University of Electronic Science and Technology of China, 2006 Xiyuan Ave, West High-Tech Zone, Chengdu, 611731, P. R. China. E-mail: mwu@uestc.edu.cn

† Electronic supplementary information (ESI) available. See DOI: 10.1039/d1ra01561c

for the preparation of LLMO materials with high electrochemical properties.

Herein, we provide a strategy to synthesize unique core–shell SCMO@LLMO composite cathodes by the growing nano-SCMO shell *in situ* on the LLMO. The particle-and-sheet composite nano-SCMO shell increases the contact area between the material and the electrolyte and exhibits good structural stability during the charge and discharge process. In the cycling process, the SCMO shell gradually combines with the LLMO bulk phase and provides structural protection for the LLMO cathode without cracking and peeling, demonstrating good material compatibility. As a result, SCMO@LLMO exhibits a good initial CE, rate performance, and cyclic stability, making it an excellent high-performance cathode for LIBs compared with other modification methods (Table S1, ESI†). In addition, the experimental results are supported well by density functional theory (DFT) and *in situ* X-ray diffraction (*in situ* XRD), *in situ* differential electrochemical mass spectrometry (*in situ* DEMS) measurements. Overall, the experimental scheme is simple and effective, making it promising for wide applicability.

2. Experimental

2.1 Material synthesis

All chemicals are of analytical grade. LLMO ($Li_{1.2}Mn_{0.54}Ni_{0.13}Co_{0.13}O_2$) was prepared by co-precipitation.[38] All of the experimental procedures described below were performed under continuous nitrogen (N_2) protection except step (4). The typical synthesis route is as follows:

(1) Pretreatment. $Mn(OH)_2$ (Sigma-Aldrich LLC, 99.99%) and LLMO materials at a molar ratio of 1.3 : 1 were mixed with 25 mL deionized water for 1 h. Ultrasonic dispersion of the stirred $Mn(OH)_2$ mixture was conducted for 30 min, and a peristaltic pump was used to add the LLMO cathode material mixture dropwise under high-speed stirring. Stirring continued for 2 h to obtain the pre-treated mixture.

(2) Acid treatment. 2.67 mL of 70% dilute H_2SO_4 (Sigma-Aldrich LLC, 99.999%) solution was added dropwise into the pre-treated mixture. The mixture was stirred at 80 °C at a constant speed for 1 h. Then, 2 g polyvinylpyrrolidone (PVP, Sigma-Aldrich LLC, average mol. wt 40 000) was added. Stirring continued at 80 °C at a constant speed for 0.5 h to obtain the acid-treated mixture.

(3) Hydrothermal. 20 mL of $KMnO_4$ (Sigma-Aldrich LLC, ACS reagent, ≥99.0%) solutions at concentrations ranging from 0.5–2.5 M (the samples are denoted as SCMO@LLMO-0.5, SCMO@LLMO-1.0, SCMO@LLMO-1.5, SCMO@LLMO-2.0, and SCMO@LLMO-2.5) were prepared. Then, the mixed solution with acid treatment was added dropwise, and the mixture was stirred at 80 °C at a constant speed for 5 min. Then, the mixed solution was transferred to a 100 mL polytetrafluoroethylene hydrothermal reaction kettle and placed in the oven. The temperature of the oven was increased from 80 °C to 140 °C at a rate of 0.5 °C min^{-1} and baked for 12 hours.

(4) Calcination. The hydrothermal products were washed, filtered, and placed in a muffle furnace at 300 °C for 5 h at a heating rate of 2 °C min^{-1} to obtain the target products.

2.2 Material characterizations

Field emission scanning electron microscopy (FE-SEM, FEI Inspect F50) was used to characterize the morphology of the coated samples at different cycling stages. The elemental composition of the SCMO@LLMO was analyzed by energy-dispersive X-ray spectroscopy (EDS) using the same FE-SEM. The elemental Mn quantity of samples with different shell thicknesses was quantitatively analyzed by inductively-coupled plasma spectrometry (ICP-OES, Agilent 7800 ICP-MS). Transmission electron microscopy (TEM, FEI Tecnai G2 F30) was used to measure the thickness of the shell at an accelerating voltage of 300 kV. High-resolution transmission electron microscopy (HRTEM) was used to measure the lattice spacing of the samples. The diffraction patterns were observed *via* selected electron diffraction (SEAD) images. The specific surface area (BET) and the pore size distribution ratio of SCMO@LLMO-2.0 and LLMO were tested by JWEB SCI. & TECH. JW-BK10C specific surface area analyzers. The structure of the sample was analyzed by powder X-ray diffractometry (XRD, PANalytical X-ray Diffractometer Model X'pert 3, Cu-Kα radiation: $\lambda = 1.5406$ Å, 2° min^{-1}, 10–120°). The *in situ* XRD (Bruker D8 Advance ECO, 10° min^{-1}, 15–72°) was performed at 2.5–4.8 V and 0.1C. The *in situ* XRD cell used a half-cell in 2.3(1). The *in situ* XRD device consisted of a Cu-made base and a cover with a sealed Be ring allowing penetration of the X-rays through and an electrode plate soaked in electrolyte. Cu-Kα ($\lambda = 1.5418$ Å) was used as source and a scan rate of 20° min^{-1}. X-ray photoelectron spectroscopy (XPS, Thermo Scientific K-Alpha) with a MgKα excitation source (1253.6 eV) was used to measure the percent of element valence.

2.3 Electrochemical measurements

(1) Half-cell. All electrochemical performance was tested with a CR-2032 half-cell at room temperature. The slurry was prepared using the active material (80 wt%), carbon black (Super P, 10 wt%), and polyvinylidene fluoride (PVDF, 10 wt%). The slurry was coated on the Al foil (Al has no contribution to the capacity[39] and the shell thickness is 150 μm). The half-cell used pure Li foil as the cathode. The electrolyte was 1 M $LiPF_6$ in a cosolvent of ethyl carbonate (EC), dimethyl carbonate (DMC), and ethyl methyl carbonate (EMC) (1 : 1 : 1 in volume). Celgard 2400 (25 μm) was used as a separator for cell assembly. The LAND cell test system (CT2001A LAND) was used for charge/discharge. Cyclic voltammograms (CV, 2.5–4.8 V, 0.5 mV s^{-1}) were measured at a CHI660E electrochemical workstation, and electrochemical impedance (EIS) curves were measured at frequencies ranging from 0.01 to 100k Hz.

(2) Full-battery. Graphite (96.5 wt%), sodium carboxymethyl cellulose (CMC, 1.5 wt%), Super P (0.5 wt%), and styrene-butadiene rubber (SBR, 1.5 wt%) were prepared as a mixed slurry. Then, the slurry was coated on the Cu foil. After drying for 8 h in a vacuum oven at 80 °C, the as-prepared electrode was used as the full battery.

3. DFT methods

The SCMO$(Li_2O)_x$ ($x \approx 1$, 010 crystal plane), SCMO$(Li_2O)_x$ ($x \approx 0$, 001 crystal plane) and LLMO (100 crystal plane) surfaces were

adopted as active surfaces to simulate the Li^+ diffusion process. We used 2 × 1, 1 × 1 and 2 × 1 super cells containing six, five and nine atomic layers for SCMO$(Li_2O)_x$ ($x \approx 1$, 010 crystal plane), SCMO$(Li_2O)_x$ ($x \approx 0$, 001 crystal plane) and LLMO (100 crystal plane) respectively. As shown in Fig. S6,† 10 Mn atoms were replaced by 3 Co, 3 Ni and 4 Li atoms in the LLMO (100 crystal plane) supercell, to reach an atoms stoichiometries. The height of supercell is set as 15 Å to insure negligible interaction between adjacent slabs.

The first-principles density functional calculations were using Perdew–Burke–Ernzerhof (PBE)[40] functional within the spin-polarized GGA+U approximation as implemented in the Cambridge serial total energy package (CASTEP)[41] code. The Vanderbilt ultrasoft pseudopotential[42] was used with a cutoff energy of 450 eV. Geometric convergence tolerances were set for maximum force of 0.03 eV $Å^{-1}$, maximum energy change of 10–5 eV per atom, maximum displacement of 0.001 Å and maximum stress of 0.5 GPa. Density mixing electronic minimisation was implemented and the self-consistent field (SCF) tolerance was set to "fine" with high accuracy of 10–6 eV per atom for energy convergence. The Hubbard U correction was introduced to describe the effect of localized d electrons of the transition metal ions. The applied effective U value was taken from previous theoretical reports: 5.0 eV, 4.0 eV, 6.4 eV for Mn, Co, Ni respectively.[43–46] The migration barriers of the Li-ion in the material are calculated using the NEB method as implemented in CASTEP.

The diffusion of Li was investigated by searching the possible diffusion route and identifying the migration transition state with the lowest diffusion energy barrier. The diffusion energy barrier is the energy difference between the total energies of transition state and the initial structure. The transition state is searched by the generalized synchronous transit (LST/QST) method implemented in the CASTEP code. The algorithm starts from a linear synchronous transit (LST) optimization, and continues with a quadratic synchronous transit (QST) maximization process. Thereafter, the conjugate gradient (CG) minimization is conducted from the obtained LST/QST structure to refine the geometry of transition state. The LST/QST/CG calculations are repeated till a stable transition state is obtained.

4. Results and discussion

4.1 Synthesis of SCMO@LLMO

As shown in Fig. 1a and Table S2,† the synthesis of SCMO@LLMO can be divided into four stages: pretreatment, acid treatment, hydrothermal, and calcining. In the pre-coating stage, the $Mn(OH)_2$ protective layer is coated onto the surface so as to protect the structure of LLMO.[47,48] Subsequently, dilute sulfuric acid and PVP are added to construct $MnSO_4$, providing hydrothermal reaction sites on the surface of the $Mn(OH)_2$ protective layer. Then, the material is heated at 140 °C for 12 h, during which the reduction of the Mn^{7+} and particle SCMO (p-SCMO) structure occurs. H_2SO_4 is continuously generated and it reacts with the $Mn(OH)_2$ protective layer to produce $MnSO_4$, providing reactants for the continuous hydrothermal process. The $KMnO_4$ concentration determines the thickness of the SCMO shell during the hydrothermal process and the thickness of the $Mn(OH)_2$ protective layer after the hydrothermal process. Excess $Mn(OH)_2$ is calcined at 300 °C for 5 h to transform into sheet SCMO (s-SCMO). The above treatment can grow an SCMO shell on the LLMO surface *in situ* without damaging the bulk phase. This method does not need to be synthesized from the precursor stage of the LLMO and provides a new method for large-scale synthesis of high-performance SCMO@LLMO cathodes.

4.2 Material characterization

In order to explore the influence of the SCMO shell on the microstructure and composition of the SCMO@LLMO material, the morphology and surface components of the samples were characterized by FE-SEM, EDS, TEM, SEAD, and ICP-OES.

As shown in Fig. 1b–e, the uncoated secondary LLMO particles (Fig. 1b) are micro-spheres of diameter of 5–10 μm. The primary particles are regular hexagonal massive particles with a uniform particle size of 200 nm (Fig. 1c), and the surface has uniform distribution holes (Fig. S1a and b†). Compared with LLMO, the secondary particle size of the coated layer (Fig. 1d) does not change significantly, but the surface of the material exhibits a distinct petal-like structure (Fig. S1c and d†). Fig. 1e shows that the SCMO shell is composed of two-type SCMO: one is the compact petal-like s-SCMO (200–300 nm) on the outermost layer, and the other is the p-SCMO (10–20 nm) on the inner layer. The p-SCMO on the inner layer of nano particles are needed to improve battery performance as found by others.[49] As shown in Table S3,† the specific surface area (BET) increases from approximate 75.227 $m^2 g^{-1}$ (the LLMO) to 96.475 $m^2 g^{-1}$ (the SCMO@LLMO-2.0) due to the introduction of nano-SCMO shell. The two-type SCMO coating structure increases the contact area between the electrode/electrolyte of SCMO@LLMO-2.0, improving the electrochemical reaction.[50] The pore size distribution ratio provided in Table S3† indicates the nano-porous characteristics of the LLMO and SCMO@LLMO. The existence of numerous nano-porous is beneficial for electrolytes to contact with the porous structure of cathode, which results in increasement of capacity during the Li^+ insertion/extraction processes. SCMO@LLMO has higher 1–5 nm pore size distribution ratio (96.2%) than LLMO (89.6%), which explains that SCMO@LLMO has more Li^+ diffusion tunnels, leading to better electrochemical performance.[51]

TEM images verify the above conclusions (Fig. 1f and j). The SCMO shell is seen on the SCMO@LLMO and exhibits a particle-and-sheet composite structure (Fig. S1f†). Furthermore, HRTEM was used to study changes in the crystal structure (Fig. S1e†). The LLMO had a clear lattice fringe with a spacing of 0.4045 nm (003). Both of the structures of the SCMO shell have clear and bright lattice fringes (Fig. 1g and k). As shown in Fig. 1h and l, the lattice spacing of the s-SCMO is 0.223 nm (300), and the lattice spacing of the inner p-SCMO is 0.307 nm (310). The SEAD performed randomly on p-SCMO and s-SCMO indicates that the two types of MnO_2 are both single-crystal phases (inset of Fig. 1g and k). The EDS results indicate

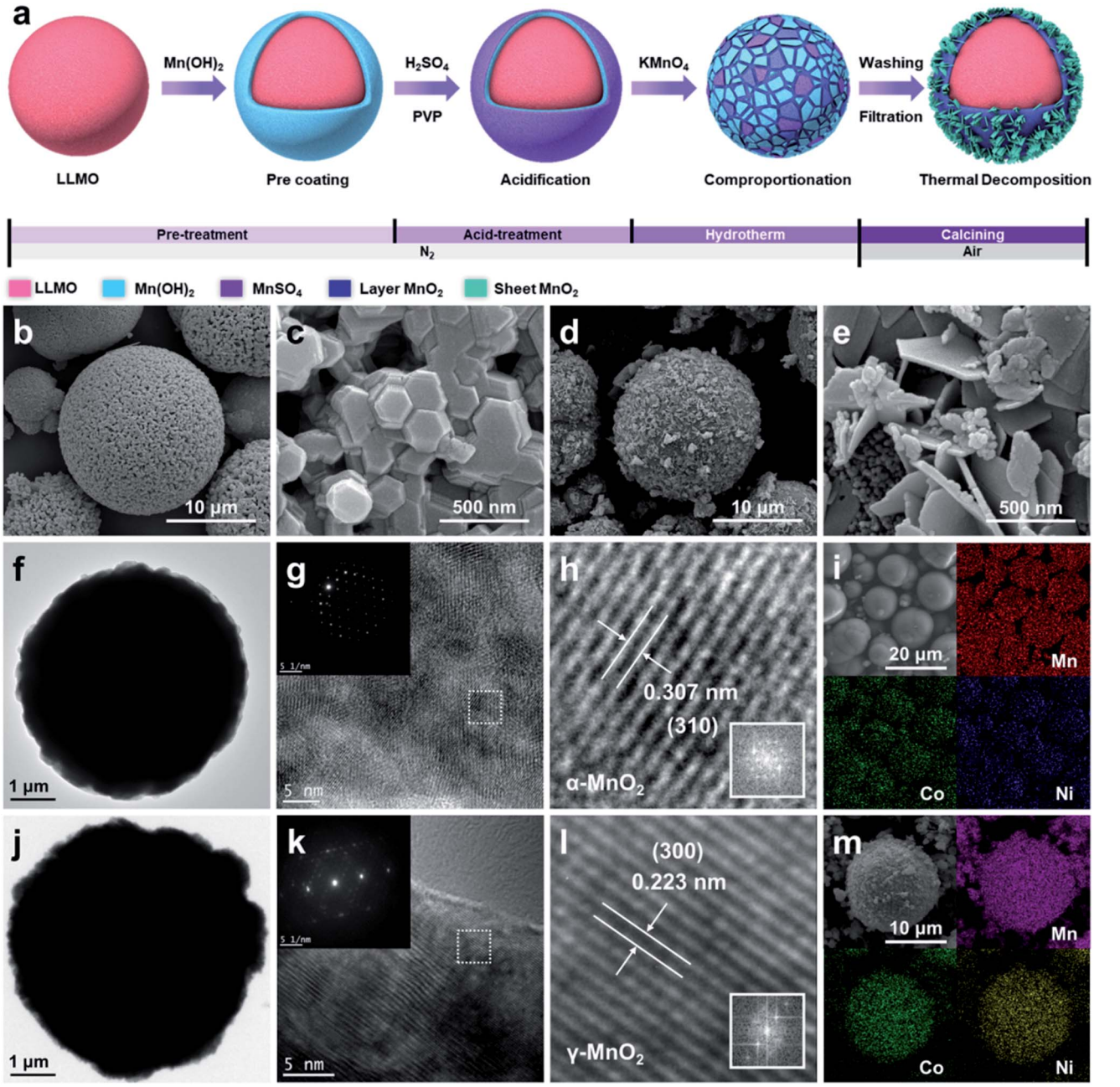

Fig. 1 (a) The synthesis strategy of SCMO@LLMO cathode, (b–e) SEM images of LLMO and SCMO@LLMO, (f and j) TEM images of LLMO and SCMO@LLMO, (g, h, k and l) HRTEM images of SCMO@LLMO, (i and m) EDS mapping images of LLMO and SCMO@LLMO.

a uniform distribution of Mn, Ni, and Co elements on the surface of the LLMO (Fig. 1i and S1g, h†). The atomic ratio is approximately 4 : 1 : 1, which matches well with the elemental ratio of LLMO. The proportion of Mn in SCMO@LLMO is increased (Fig. S1j†), indicating that the uniform coating of MnO_2 does not affect the elemental distribution in LLMO (Fig. 1m and S1i†). The ICP-OES results (Fig. S1k†) quantitatively prove that the element ratio of Mn, Co, and Ni is 4 : 1 : 1, the content of MnO_2 in the sample increased with the $KMnO_4$ concentration, and the SCMO shell gradually thickened.

Powder XRD was carried out to explore the effects of SCMO@LLMO preparation with different $KMnO_4$ concentrations (SCMO@LLMOs). As shown in Fig. 2a, the SCMO@LLMO samples obtained using different $KMnO_4$ concentrations exhibit a Li_2MnO_3 component superlattice diffraction peak in the range of 20° to 25° (in contrast to standard PDF #01-070-4311). LLMO contains the *C*2/*m* space group of a monoclinic crystal system, and the other peaks of all the samples are consistent with the standard PDF card, indicating that the synthesis process does not cause damage to the structure of LLMO owing to the $Mn(OH)_2$ protection layer.[52,53]

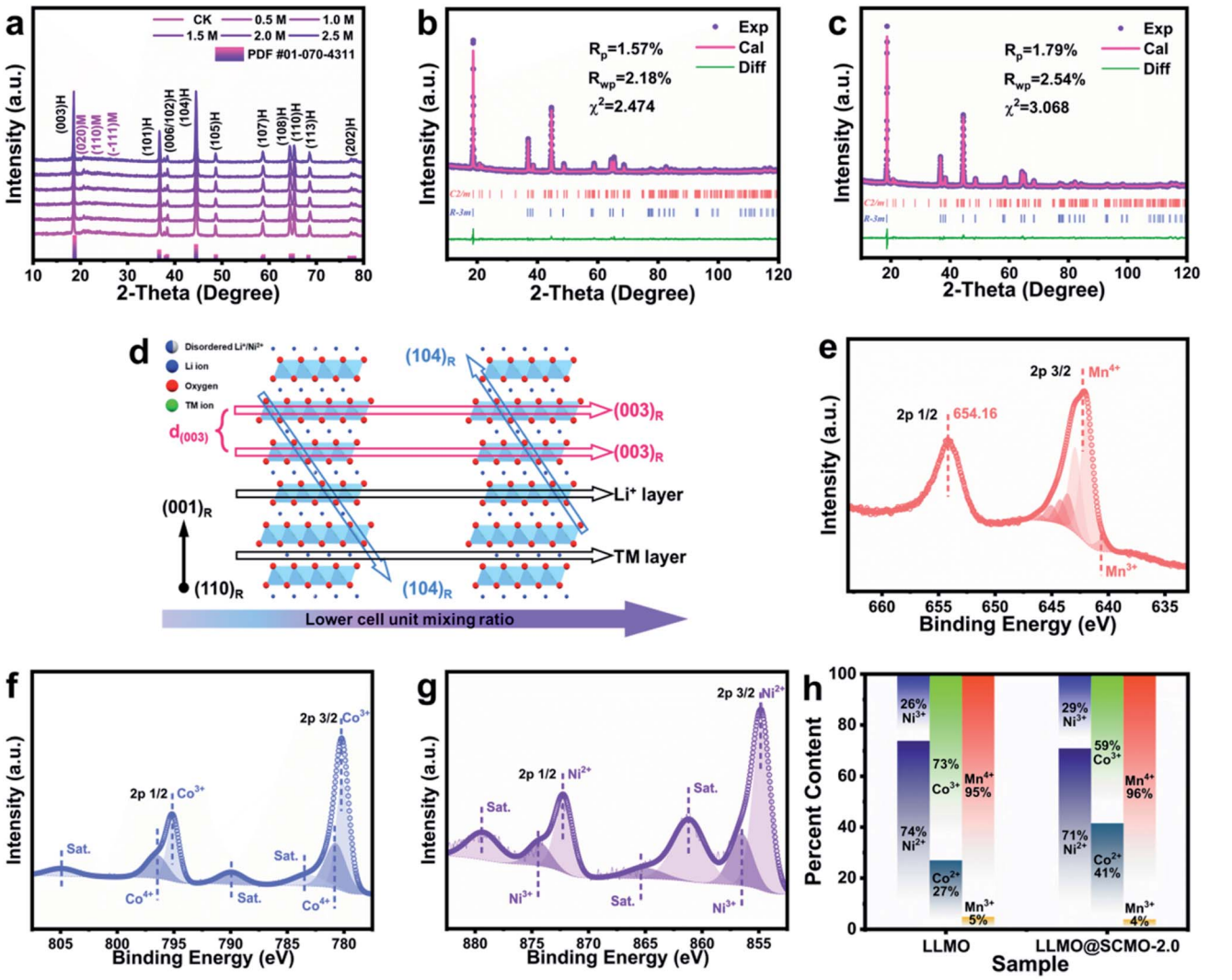

Fig. 2 (a) The X-ray diffraction patterns of SCMO@LLMOs, (b and c) the XRD Rietveld refinement images of LLMO and SCMO@LLMO-2.0, (d) the image of SCMO@LLMO-2.0 lower cell Li^+/Ni^{2+} mixing ratio mechanism, (e–g) the XPS (Ni, Co and Mn) of SCMO@LLMO-2.0, (h) XPS peak fitting of LLMO and SCMO@LLMO-2.0.

As shown in Fig. 2b and c, The XRD curves of LLMO and SCMO@LLMO are refined (XRD Rietveld refinement, Table S4†).[54,55] The values of *c*/*a* for LLMO and SCMO@LLMO are 5.034466955 and 5.002496091, respectively, which are greater than 5. This indicates that the layered structure of the two samples fully developed and the SCMO shell effectively protects the structure. Secondly, the LLMO exhibits a more serious degree of Li^+/Ni^{2+} mixing. The proportion of LLMO crystal cell unit mixing is 3.09%, while the value of 3*b* of Li replaced by Ni in SCMO@LLMO is 0 due to hydrothermal reaction. The lower Li^+/Ni^{2+} mixing degree results in a larger cell volume for the $LiTMO_2$ (TM = transition metal) phase and significantly increases the average cell volume of the $LiTMO_2$ and Li_2MnO_3 two-phase composite, which provides more Li^+ diffusion channels. The SCMO@LLMO still maintains a high *c*/*a* value, which indicates that the SCMO@LLMO has a large (003) layer spacing corresponding to the Li^+ diffusion channel. The single crystallization process maintains the original large Li^+ diffusion channel of the material, improving the rate performance of SCMO@LLMO (Fig. 2d).

XPS was used to study the element valence of the samples. As shown in Fig. 2e–g and S2,† the Ni, Co, and Mn peaks did not change significantly before and after coating. After peak fitting (Fig. 2h and Table S5†), the valence states of Ni, Co, and Mn elements remained relatively stable. The content ratio of Mn^{4+} increased after coating, indicating that a small amount of MnO_2 is coated onto the LLMO. In addition, the proportion of Ni^{2+} decreases after coating. Because the radius of Ni^{2+} is close to that of Li^+, a reduction in Ni^{2+} can reduce the degree of cation mixing in the material,[56] decrease the resistance of the Li^+ insertion/extraction process, and improve the cycling performance of the material.[57] The increased Mn^{4+} proportion in SCMO@LLMO inhibits the dissolution of Mn^{x+} ($x < 4$).[58] The lattice distortion caused by the Jahn–Teller effect is also effectively inhibited.[59,60] Importantly, Mn^{4+} plays a crucial role in maintaining the cycling performance of LLMO,[61–63] as evidenced below.

4.3 Electrochemical performance

In order to characterize the electrochemical performance of LLMO and SCMO@LLMO, a CR-2032 coin half-cell was assembled for testing. As shown in Fig. 3a and S3a,† the CV curves of LLMO and SCMO@LLMO-2.0 were measured within the voltage range of 2.5–4.8 V. LLMO exhibits obvious oxidation peaks around 4.2 V and 4.6 V. The oxidation peak at 4.6 V disappeared from the second circle, indicating that the material has irreversible Li^+ and oxygen loss during the first charge and discharge process. The CV curve of SCMO@LLMO-2.0 has a similar oxidation peak as LLMO, but the oxidation peak decreases at 4.2 V indicating that the SCMO shell reduces the irreversible loss of TM and Li_2O during the cycling process. In addition, two small reduction peaks near 3.2 V indicate that Li^+ enters the two forms of SCMO to form an $R\bar{3}m$ structure in the first charge and discharge process.[64] Subsequent CV curves are more consistent than those of LLMO, indicating that the SCMO shell improves the cycling performance of the material.

Fig. 3b and S3b† show the initial charge and discharge curves of SCMO@LLMOs at a current density of 0.05C. The charging curves of all samples exhibit a voltage slope between 2.5–4.5 V and a voltage platform between 4.5–4.8 V.[65] The discharge curves of all samples are downward-sloped curves, which is consistent with the charge–discharge curve characteristics of LLMO. The initial CE of LLMO is 86.5%, while the initial CE of SCMO@LLMO increases with the $KMnO_4$ concentration. SCMO@LLMO-2.0 has the best initial CE (93.0%) due to the excellent structural stability and Li storage performance on the surface of the SCMO shell.[66] The SCMO shell inhibits the irreversible loss of oxygen and Li^+ on the surface of LLMO during the initial charge and discharge process and greatly improves the initial CE of the material. Compared with the LLMO, the SCMO@LLMO curve exhibits a platform near 3.2 V. As the $KMnO_4$ concentration increased, the length of the platform gradually increased and the discharge voltage platform gradually decreased. The reduction peak near 3.1 V in the

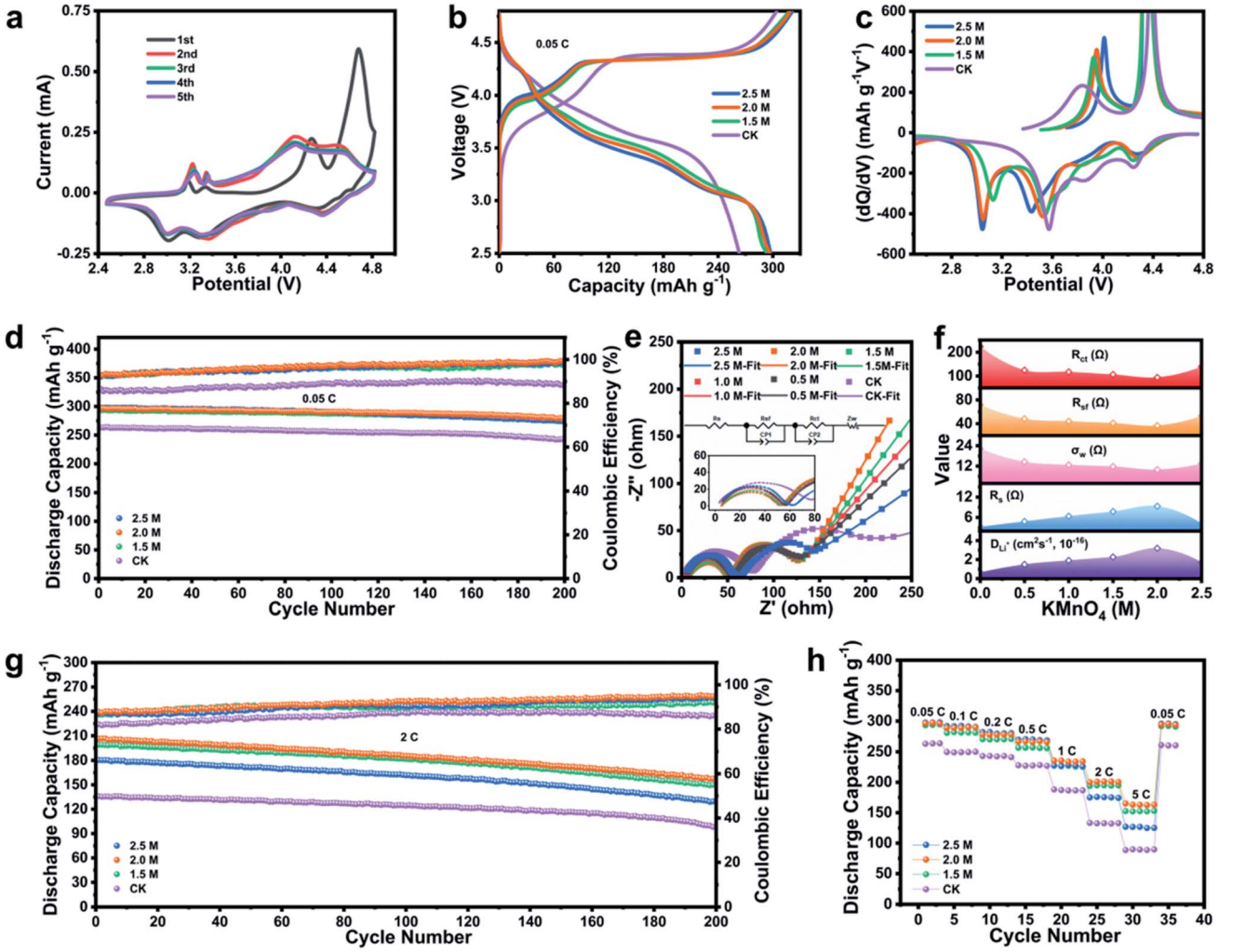

Fig. 3 (a) CV curves of SCMO@LLMO-2.0, (b) the initial charge and discharge curve of SCMO@LLMOs under current density of 0.05C, (c) the capacity differential curve of (b), (d and g) the cycling performance curves of SCMO@LLMOs under current densities of 0.05C and 2C, (e) Nyquist plots of the SCMO@LLMOs after 100 cycles, (f) the trends of electrochemical impedance of the SCMO@LLMOs after 100 cycles, (h) the rate performance curve of SCMO@LLMOs under current densities of 0.05C, 0.1C, 0.2C, 0.5C, 1C, 2C, and 5C, respectively.

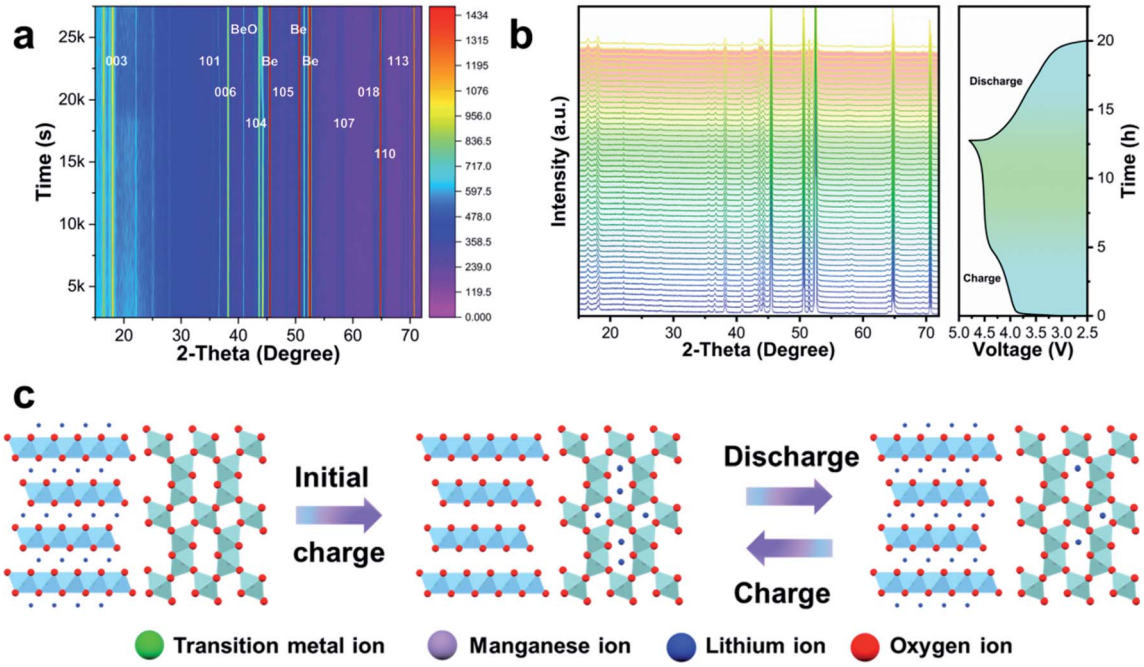

Fig. 4 (a) Contour map of *in situ* XRD, (b) *in situ* X-ray diffraction patterns of SCMO@LLMO-2.0 at 0.1C, (c) the action mechanism of SCMO coating layer as Li storage.

corresponding capacity differential (dQ/dV) curves (Fig. 3c and S3c†) decreases, which indicates that a certain amount of Li^+ is stored in the SCMO shell during the discharge process, improving the initial CE.[67]

Fig. S4a† shows the EIS curves of SCMO@LLMOs before cycling. The SCMO@LLMO-2.0 electrode has the lowest impedance of the diffusion migration resistance (R_{sf}, 30.32 Ω) and the charge transfer resistance (R_{ct}, 85.71 Ω). Under a current density of 0.05C (Fig. 3d), SCMO@LLMO-2.0 has the best cycling performance. Its initial CE is 93.0% and its initial discharge capacity is 296.9 mA h g^{-1}. The capacity retention rate of SCMO@LLMO-2.0 is still 93.9% after 200 cycles. For comparison, LLMO exhibits an initial CE of 86.5% and an initial discharge capacity of 263.2 mA h g^{-1}, and the capacity retention rate is 91.8% after 200 cycles. Thus, the cycling performance of SCMO@LLMOs increased with the concentration of $KMnO_4$. The higher proportion of Mn^{4+} in the SCMO shell inhibited the dissolution of low-valence Mn in the cycling process[68] and also hindered lattice distortion. Moreover, the reduced Ni^{2+} proportion inhibited the cation mixing degree, improving the cycling performance.

Notably, SCMO@LLMO-2.5 has a higher capacity in the first 80 cycles at a low rate (Fig. 3d and S5a–d†). Under a high rate (Fig. 3g and S5e–g†), the capacity retention rate gradually decreases with discharge capacity reduction. The capacity retention rates after 100 cycles are 92.84%, 89.59%, 81.14%, and the retention rates after 200 cycles are 81.35%, 71.48%, 56.43% for SCMO@LLMO-2.5 at 1C, 2C, and 5C, respectively. The cycling performance of SCMO@LLMO-2.5 is slightly better than that of SCMO@LLMO-2.0 due to the excess thickness of the SCMO shell, which extends the migration path of Li^+ in the cycling process and results in the failure of Li^+ to fully re-insert into the LLMO phase. Finally, this leads to the destruction of the structure and the attenuation of capacity. This is because the thickness of the SCMO shell generated under 2 M $KMnO_4$ inhibits the irreversible loss of Li^+ while allowing enough Li^+ to be re-inserted into LLMO to maintain the structural stability of the material.

Further EIS tests were performed on the SCMO@LLMO-2.0 electrode after 100 cycles (Fig. 3e, f and Table S6†). The results show that the SCMO@LLMO-2.0 electrode still has the highest Li^+ diffusivity of 3.19×10^{-16} cm^2 s^{-1}, which crucial to its optimal cycling performance. As shown in the fitting diagram and the equivalent circuit diagram, the R_{sf} and the R_{ct} of LLMO are both higher than SCMO@LLMO. This indicates that the surface structure of LLMO collapses after 100 cycles, and the disordered surface structure hinders the migration of Li^+ and intensifies the resistance in the process of insertion/extraction. Compared with LLMO, SCMO@LLMO has a larger Li^+ diffusion coefficient, which is related to the stable surface structure and the larger (003)R layer spacing. The single-crystal layer provides a channel for charge transport, making the Li^+ insertion/extraction process in the material smoother.

Fig. S4b–d† show the EIS curves of SCMO@LLMO-2.0 and LLMO after different cycles (0, 50, 100, 150, and 200 cycles). The small impedance variation of SCMO@LLMO-2.0 compared to LLMO is another important reason for its superior electrochemical performance. Additionally, the trend of the Li^+ diffusion coefficient with the $KMnO_4$ concentration in Fig. 3f further proves the capacity attenuation of SCMO@LLMO-2.5.

After verifying the cycling performance of SCMO@LLMO electrodes at a high rate of 2C, SCMO@LLMO-2.0 still exhibits

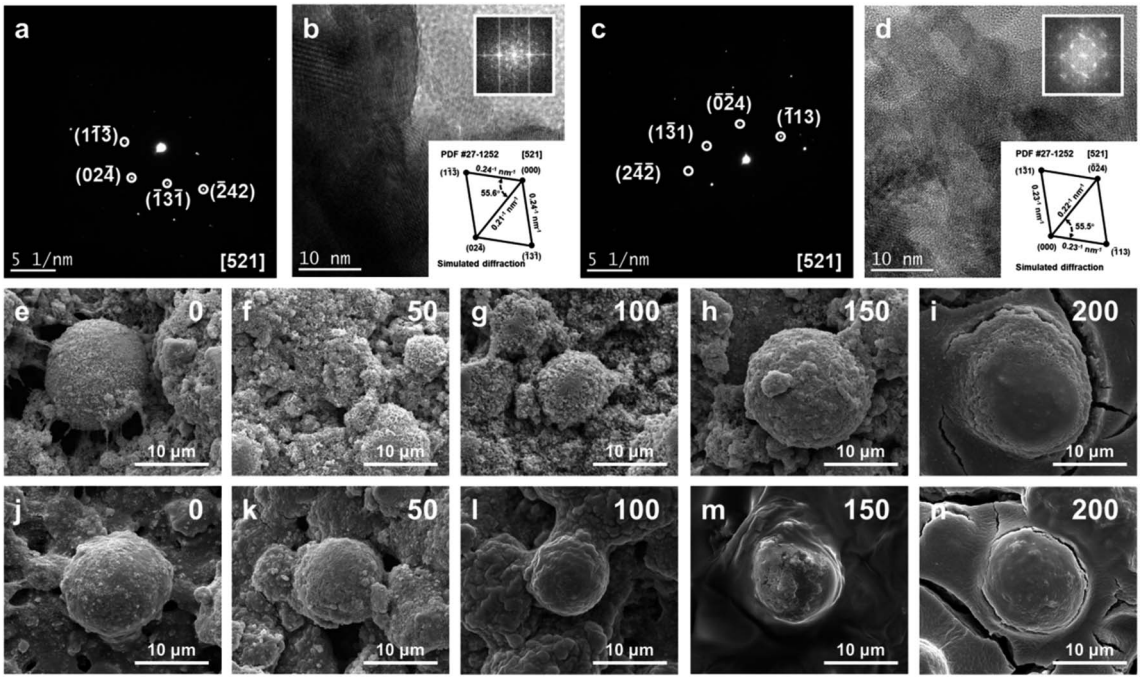

Fig. 5 (a and c) SEAD of p-SCMO and s-SCMO after 50 cycles, (b and d) HRTEM of p-SCMO and s-SCMO after 50 cycles, (e–n) SEM images of SCMO@LLMO-2.0 and LLMO at 2C after 0, 50, 100, 150, and 200 cycles, respectively.

the best initial CE (87.7%), the highest discharge specific capacity (206.5 mA h g^{-1}), and the best capacity retention rate (76.0%) after 200 cycles (Fig. 3g).

Fig. 3h and S5h† compare the rate performance of SCMO@LLMOs. SCMO@LLMO-2.0 shows the best rate performance. The discharge capacities are 296.3, 288.9, 278.0, 266.4, 235.4, 200.0, and 165.0 mA h g^{-1}, respectively, at current densities of 0.05, 0.1, 0.2, 0.5, 1, 2 and 5C. As a comparison, the discharge capacities of LLMO under the same current densities are 262.7, 249.5, 243.0, 227.8, 188.1, 133.1 and 88.6 mA h g^{-1}, respectively, further demonstrating that SCMO@LLMO-2.0 has the best electrochemical performance. In summary, SCMO@LLMO-2.0 electrode has good electrochemical performance, which making it an excellent cathode for LIBs compared with other materials (Table S1†).

In order to further explore the change of the SCMO@LLMO-2.0 structure during the initial charge and discharge process, *in situ* XRD was carried out on the SCMO@LLMO-2.0 electrode. As shown in Fig. 4, each main peak does not deviate significantly during the initial charge and discharge process, indicating that Li_2O disassembly only has a slight impact on the structure of SCMO@LLMO-2.0 and the overall structure of the material remained stable. Thus, we inferred that, compared with LLMO, SCMO@LLMO-2.0 exhibits a higher initial CE due to its stable surface structure. In addition, the excellent Li storage performance of the SCMO shell prevents irreversible Li^+ loss during the initial charge and discharge process. The *in situ* XRD contour map reflects the position changes of each diffraction peak in the initial charge and discharge process more intuitively, confirming the above electrochemical performance conclusions.

In order to better observe morphological changes in the material during the cycling process, TEM and SEM were carried out on the samples after charge and discharge. Fig. 5a–d show TEM images of SCMO@LLMO-2.0 after 50 cycles. Surprisingly, a single-crystal shell of a Li_2MnO_3 monoclinal crystal system ($C2/m$) was observed, demonstrating good material compatibility with LLMO, which indicates that the SCMO shell does inhibit the irreversible loss of Li_2O and retains Li^+. Fig. 5e–i compare the SEM images of SCMO@LLMO-2.0 after 0, 50, 100, 150, and 200 cycles, respectively, under a current density of 2C. Compared to the SEM images of LLMO (Fig. 5j–n) under the same test conditions, the SCMO shell of SCMO@LLMO-2.0 did not peel or crack from the bulk phase. The SCMO shell gradually becomes a part of the LLMO phase structure during the cycling process, indicating that SCMO@LLMO-2.0 maintains good stability in the charging and discharging process.

In order to explore the application of SCMO@LLMO-2.0 in a full battery, commercial graphite and SCMO@LLMO-2.0 were used as the electrode materials for assembling a full battery.

As shown in Fig. 6a, SCMO@LLMO-2.0 has a higher initial discharge specific capacity (191.3 mA h g^{-1}) and better initial CE (84.7%) than the LLMO cathode (124.8 mA h g^{-1}, 81.4%). Moreover, SCMO@LLMO-2.0 exhibits better rate performance than LLMO under various current densities (Fig. 6b). The capacity retention rate of SCMO@LLMO-2.0 (70.6%) is higher than LLMO (67.0%) after 200 cycles, showing excellent cycling performance (Fig. 6c).

5. First-principle calculations

Fig. 7 and S6† show the Li migration barriers, diffusion paths and migration models of LLMO and SCMO shell after first-

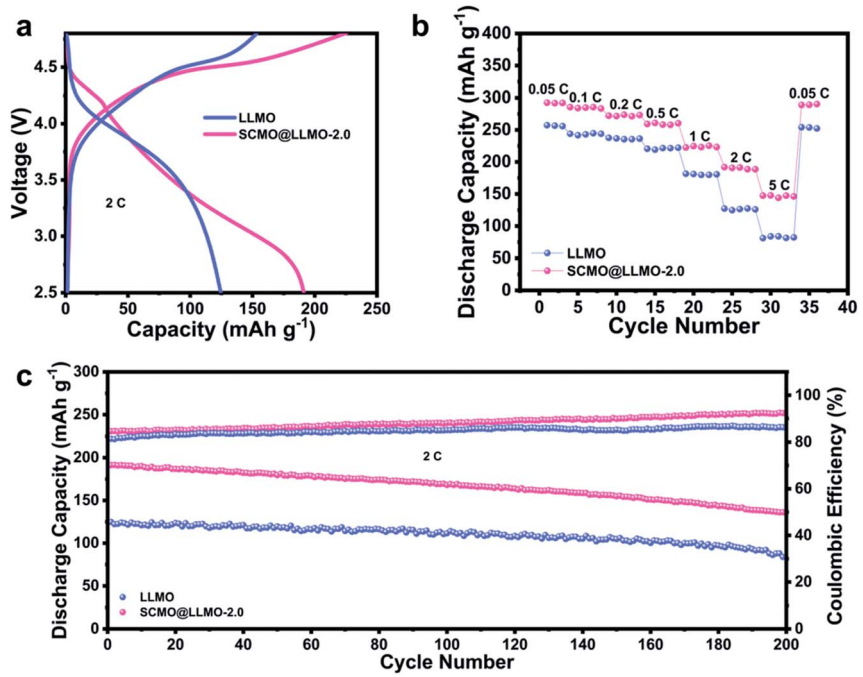

Fig. 6 (a) The initial charge and discharge curves of LLMO and SCMO@LLMO-2.0 full cells under current density of 2C, (b) the rate performance curves of LLMO and SCMO@LLMO-2.0 full cells under current densities of 0.05C, 0.1C, 0.2C, 0.5C, 1C, 2C, and 5C, respectively, (c) the cycling performance curves of LLMO and SCMO@LLMO-2.0 under current densities of 2C.

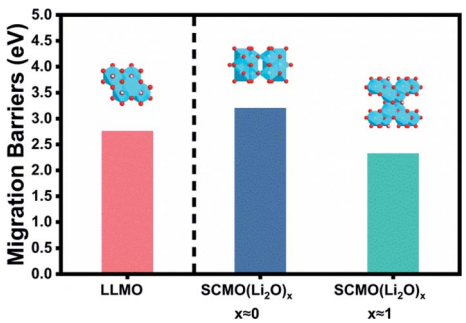

Fig. 7 Li migration barriers of LLMO and SCMO(Li_2O)$_x$.

principle calculations. Calculations showed that SCMO shell at the start of cycling ($x \approx 0$) had a higher Li migration barrier than LLMO, which indicates that the SCMO shell does inhibit the irreversible loss of Li during the initial cycling. Moreover, SCMO shell during cycling ($x \approx 1$) had a lower Li migration barrier than LLMO, indicating SCMO shell does has excellent cycling performance. The calculation results showed that the theoretical results of SCMO shell modification can be basically consistent with the experimental results.

6. Conclusions

In summary, an SCMO shell was designed, synthesized, and coated onto LLMO. The SCMO shell was grown *in situ* on the surface of LLMO and exhibits a unique particle-and-sheet composite morphology. The unique two-type SCMO structure provides greater electrode/electrolyte contact area, better bulk phase material protection, and a more stable surface structure and inhibits lattice distortion and Li^+/Ni^{2+} mixing. These positive effects, in addition to the excellent Li^+ migration and storage mechanism of the SCMO shell, greatly improved the electrochemical properties of the materials. For a half-cell at 0.05C, the initial CE and initial discharge capacity of SCMO@LLMO-2.0 was 93.0% and 296.9 mA h g^{-1}, the capacity retention rate of SCMO@LLMO-2.0 was 93.9% after 200 cycles. For a full battery, the SCMO@LLMO-2.0 exhibits a good initial CE (191.3 mA h g^{-1}, 84.7%) and cycling performance (100 cycles 87.9%, 200 cycles 70.6%) under a current density of 2C. *In situ* XRD, *in situ* DEMS tests and DFT calculations demonstrated that SCMO has excellent structural stability and a lower Li^+ migration barrier. This work provides a new scheme and theoretical support for the modification of LLMO, and the prepared SCMO@LLMO-2.0 has great commercial primary batteries application potential.

Conflicts of interest

There are no conflicts to declare.

Acknowledgements

This work was financially supported by the Chengdu Science and Technology Bureau (2019YFG0526/2020YFG0339) and the Science and Technology Department of Sichuan province (2019YFH0002/2020YFH0097). This research thanks Prof. Hongyan Wang at School of Physical Science and Technology,

Key Laboratory of Advanced Technology of Materials, Ministry of Education of China, Southwest Jiaotong University, Chengdu 610031, China for her support of the DFT calculations, the CASTEP software copyright belongs to the key laboratory. The authors gratefully acknowledge the colleagues from Excellent Science and Technology Innovation Group of Jiangsu Province for their contributions in DFT calculations.

References

1 S. Zhao, Z. Guo, K. Yan, S. Wan, F. He, B. Sun and G. Wang, Towards high-energy-density lithium-ion batteries: Strategies for developing high-capacity lithium-rich cathode materials, *Energy Storage Materials*, 2021, **34**, 716–734, DOI: 10.1016/j.ensm.2020.11.008.

2 H. Zheng, X. Han, W. Guo, L. Lin, Q. Xie, P. Liu, W. He, L. Wang and D. L. Peng, Recent developments and challenges of Li-rich Mn-based cathode materials for high-energy lithium-ion batteries, *Materials Today Energy*, 2020, **18**, 100518, DOI: 10.1016/j.mtener.2020.100518.

3 Y. Li, M. J. Zuba, S. Bai, Z. W. Lebens-Higgins, B. Qiu, S. Park, Z. Liu, M. Zhang, L. F. J. Piper and Y. S. Meng, Regeneration of degraded Li-rich layered oxide materials through heat treatment-induced transition metal reordering, *Energy Storage Materials*, 2021, **35**, 99–107, DOI: 10.1016/j.ensm.2020.11.013.

4 J. Liang, L. Wen, X. Yu, F. Li and H. M. Cheng, Cathode materials: A key challenge for lithium ion batteries, *Energy Storage Materials*, 2018, **14**, A1–A3, DOI: 10.1016/j.ensm.2018.07.027.

5 F. Friedrich, B. Strehle, A. T. S. Freiberg, K. Kleiner, S. J. Day, C. Erk, M. Piana and H. A. Gasteiger, Editors' choice—capacity fading mechanisms of NCM-811 cathodes in lithium-ion batteries studied by X-ray diffraction and other diagnostics, *J. Electrochem. Soc.*, 2019, **166**, A3760–A3774, DOI: 10.1149/2.0821915jes.

6 W. C. Chien, Y. R. Li, S. H. Wu, Y. S. Wu, Z. H. Wu, Y. J. James Li and C. C. Yang, Modifying the morphology and structure of graphene oxide provides high-performance $LiFePO_4$/C/rGO composite cathode materials, *Adv. Powder Technol.*, 2020, **31**, 4541–4551, DOI: 10.1016/j.apt.2020.10.002.

7 S. Zhao, K. Yan, J. Zhang, B. Sun and G. Wang, Reaction mechanisms of layered lithium-rich cathode materials for high-energy lithium-ion batteries, *Angew. Chem., Int. Ed.*, 2020, DOI: 10.1002/anie.202000262.

8 P. K. Nayak, E. M. Erickson, F. Schipper, T. R. Penki, N. Munichandraiah, P. Adelhelm, H. Sclar, F. Amalraj, B. Markovsky and D. Aurbach, Review on challenges and recent advances in the electrochemical performance of high capacity Li- and Mn-rich cathode materials for Li-ion batteries, *Adv. Energy Mater.*, 2018, **8**, 1–16, DOI: 10.1002/aenm.201702397.

9 M. M. Thackeray, S. H. Kang, C. S. Johnson, J. T. Vaughey, R. Benedek and S. A. Hackney, Li_2MnO_3-stabilized $LiMO_2$ (M = Mn, Ni, Co) electrodes for lithium-ion batteries, *J. Mater. Chem.*, 2007, **17**, 3112–3125, DOI: 10.1039/b702425h.

10 E. Zhao, L. He, B. Wang, X. Li, J. Zhang, Y. Wu, J. Chen, S. Zhang, T. Liang, Y. Chen, X. Yu, H. Li, L. Chen, X. Huang, H. Chen and F. Wang, Structural and mechanistic revelations on high capacity cation-disordered Li-rich oxides for rechargeable Li-ion batteries, *Energy Storage Materials*, 2019, **16**, 354–363, DOI: 10.1016/j.ensm.2018.06.016.

11 P. Yan, J. Zheng, Z. K. Tang, A. Devaraj, G. Chen, K. Amine, J. G. Zhang, L. M. Liu and C. Wang, Injection of oxygen vacancies in the bulk lattice of layered cathodes, *Nat. Nanotechnol.*, 2019, **14**, 602–608, DOI: 10.1038/s41565-019-0428-8.

12 M. Vivekanantha, T. Partheeban, T. Kesavan, C. Senthil and M. Sasidharan, Alleviating the initial coulombic efficiency loss and enhancing the electrochemical performance of $Li_{1.2}Mn_{0.54}Ni_{0.13}Co_{0.13}O_2$ using β-MnO_2, *Appl. Surf. Sci.*, 2019, **489**, 336–345, DOI: 10.1016/j.apsusc.2019.05.342.

13 Z. Zhu, R. Gao, I. Waluyo, Y. Dong, A. Hunt, J. Lee and J. Li, Stabilized Co-free Li-rich oxide cathode particles with an artificial surface prereconstruction, *Adv. Energy Mater.*, 2020, **10**, 1–11, DOI: 10.1002/aenm.202001120.

14 H. Zheng, Z. Hu, P. Liu, W. Xu, Q. Xie, W. He, Q. Luo, L. Wang, D. Gu, B. Qu, Z. Z. Zhu and D. L. Peng, Surface Ni-rich engineering towards highly stable $Li_{1.2}Mn_{0.54}Ni_{0.13}Co_{0.13}O_2$ cathode materials, *Energy Storage Materials*, 2020, **25**, 76–85, DOI: 10.1016/j.ensm.2019.10.029.

15 Rosy, S. Haber, E. Evenstein, A. Saha, O. Brontvein, Y. Kratish, D. Bravo-Zhivotovskii, Y. Apeloig, M. Leskes and M. Noked, Alkylated $Li_xSi_yO_z$ coating for stabilization of Li-rich layered oxide cathodes, *Energy Storage Materials*, 2020, **33**, 268–275, DOI: 10.1016/j.ensm.2020.08.015.

16 Y. Lei, J. Ni, Z. Hu, Z. Wang, F. Gui, B. Li, P. Ming, C. Zhang, Y. Elias, D. Aurbach and Q. Xiao, Surface modification of Li-rich Mn-based layered oxide cathodes: Challenges, materials, methods, and characterization, *Adv. Energy Mater.*, 2020, **10**, 1–27, DOI: 10.1002/aenm.202002506.

17 U. H. Kim, N.-Y. Park, G. T. Park, H. Kim, C. S. Yoon and Y. K. Sun, High-energy W-doped $Li[Ni_{0.95}Co_{0.04}Al_{0.01}]O_2$ cathodes for next-generation electric vehicles, *Energy Storage Materials*, 2020, **33**, 399–407, DOI: 10.1016/j.ensm.2020.08.013.

18 W. Jiang, C. Zhang, Y. Feng, B. Wei, L. Chen, R. Zhang, D. G. Ivey, P. Wang and W. Wei, Achieving high structure and voltage stability in cobalt-free Li-rich layered oxide cathodes via selective dual-cation doping, *Energy Storage Materials*, 2020, **32**, 37–45, DOI: 10.1016/j.ensm.2020.07.035.

19 S. Dong, Y. Zhou, C. Hai, J. Zeng, Y. Sun, Y. Shen, X. Li, X. Ren, C. Sun, G. Zhang and Z. Wu, Understanding electrochemical performance improvement with Nb doping in lithium-rich manganese-based cathode materials, *J. Power Sources*, 2020, **462**, 228185, DOI: 10.1016/j.jpowsour.2020.228185.

20 B. Li, H. Yan, J. Ma, P. Yu, D. Xia, W. Huang, W. Chu and Z. Wu, Manipulating the electronic structure of Li-rich manganese-based oxide using polyanions: Towards better

electrochemical performance, *Adv. Funct. Mater.*, 2014, **24**, 5112–5118, DOI: 10.1002/adfm.201400436.

21 Z. Ding, C. Zhang, S. Xu, J. Liu, C. Liang, L. Chen, P. Wang, D. G. Ivey, Y. Deng and W. Wei, Stable heteroepitaxial interface of Li-rich layered oxide cathodes with enhanced lithium storage, *Energy Storage Materials*, 2019, **21**, 69–76, DOI: 10.1016/j.ensm.2018.12.004.

22 Z. D. Huang, K. Zhang, T. T. Zhang, R. Q. Liu, X. J. Lin, Y. Li, T. Masese, X. Liu, X. M. Feng and Y. W. Ma, High rate and thermally stable Mn-rich concentration-gradient layered oxide microsphere cathodes for lithium-ion batteries, *Energy Storage Materials*, 2016, **5**, 205–213, DOI: 10.1016/j.ensm.2016.08.001.

23 R. A. House, G. J. Rees, M. A. Pérez-Osorio, J.-J. Marie, E. Boivin, A. W. Robertson, A. Nag, M. Garcia-Fernandez, K.-J. Zhou and P. G. Bruce, First-cycle voltage hysteresis in Li-rich 3d cathodes associated with molecular O_2 trapped in the bulk, *Nat. Energy*, 2020, **5**, 777–785, DOI: 10.1038/s41560-020-00697-2.

24 D. H. Seo, J. Lee, A. Urban, R. Malik, S. Y. Kang and G. Ceder, The structural and chemical origin of the oxygen redox activity in layered and cation-disordered Li-excess cathode materials, *Nat. Chem.*, 2016, **8**, 692–697, DOI: 10.1038/nchem.2524.

25 R. A. House, U. Maitra, M. A. Pérez-Osorio, J. G. Lozano, L. Jin, J. W. Somerville, L. C. Duda, A. Nag, A. Walters, K. J. Zhou, M. R. Roberts and P. G. Bruce, Superstructure control of first-cycle voltage hysteresis in oxygen-redox cathodes, *Nature*, 2020, **577**, 502–508, DOI: 10.1038/s41586-019-1854-3.

26 X. Li, Y. Qiao, S. Guo, K. Jiang, M. Ishida and H. Zhou, A new type of Li-rich rock-salt oxide $Li_2Ni_{1/3}Ru_{2/3}O_3$ with reversible anionic redox chemistry, *Adv. Mater.*, 2019, **31**, e1807825, DOI: 10.1002/adma.201807825.

27 Z. N. Taylor, A. J. Perez, J. A. Coca-Clemente, F. Braga, N. E. Drewett, M. J. Pitcher, W. J. Thomas, M. S. Dyer, C. Collins, M. Zanella, T. Johnson, S. Day, C. Tang, V. R. Dhanak, J. B. Claridge, L. J. Hardwick and M. J. Rosseinsky, Stabilization of O–O bonds by d^0 cations in $Li_{4+x}Ni_{1-x}WO_6$ $(0 \leq x \leq 0.25)$ rock salt oxides as the origin of large voltage hysteresis, *J. Am. Chem. Soc.*, 2019, **141**, 7333–7346, DOI: 10.1021/jacs.8b13633.

28 Y. Zuo, B. Li, N. Jiang, W. Chu, H. Zhang, R. Zou and D. Xia, A high-capacity O_2-type Li-rich cathode material with a single-layer Li_2MnO_3 superstructure, *Adv. Mater.*, 2018, **30**, e1707255, DOI: 10.1002/adma.201707255.

29 B. Li, R. Shao, H. Yan, L. An, B. Zhang, H. Wei, J. Ma, D. Xia and X. Han, Understanding the stability for Li-rich layered oxide Li_2RuO_3 cathode, *Adv. Funct. Mater.*, 2016, **26**, 1330–1337, DOI: 10.1002/adfm.201504836.

30 F. Ning, H. Shang, B. Li, N. Jiang, R. Zou and D. Xia, Surface thermodynamic stability of Li-rich Li_2MnO_3: Effect of defective graphene, *Energy Storage Materials*, 2019, **22**, 113–119, DOI: 10.1016/j.ensm.2019.01.004.

31 P. Pang, X. Tan, Z. Wang, Z. Cai, J. Nan, Z. Xing and H. Li, Crack-free single-crystal $LiNi_{0.83}Co_{0.10}Mn_{0.07}O_2$ as cycling/thermal stable cathode materials for high-voltage lithium-ion batteries, *Electrochim. Acta*, 2021, **365**, 137380, DOI: 10.1016/j.electacta.2020.137380.

32 S. H. Lee, S. J. Sim, B. S. Jin and H. S. Kim, High performance well-developed single crystal $LiNi_{0.91}Co_{0.06}Mn_{0.03}O_2$ cathode via LiCl–NaCl flux method, *Mater. Lett.*, 2020, **270**, 127615, DOI: 10.1016/j.matlet.2020.127615.

33 B. Huang, M. Wang, X. Zhang, Z. Zhao, L. Chen and Y. Gu, Synergistic coupling effect of single crystal morphology and precursor treatment of Ni-rich cathode materials, *J. Alloys Compd.*, 2020, **830**, 154619, DOI: 10.1016/j.jallcom.2020.154619.

34 C. Wang, R. Yu, S. Hwang, J. Liang, X. Li, C. Zhao, Y. Sun, J. Wang, N. Holmes, R. Li, H. Huang, S. Zhao, L. Zhang, S. Lu, D. Su and X. Sun, Single crystal cathodes enabling high-performance all-solid-state lithium-ion batteries, *Energy Storage Materials*, 2020, **30**, 98–103, DOI: 10.1016/j.ensm.2020.05.007.

35 B. Wu, H. Xu, D. Mu, L. Shi, B. Jiang, L. Gai, L. Wang, Q. Liu, L. Ben and F. Wu, Controlled solvothermal synthesis and electrochemical performance of $LiCoPO_4$ submicron single crystals as a cathode material for lithium ion batteries, *J. Power Sources*, 2016, **304**, 181–188, DOI: 10.1016/j.jpowsour.2015.11.023.

36 L. Wang, B. Wu, D. Mu, X. Liu, Y. Peng, H. Xu, Q. Liu, L. Gai and F. Wu, Single-crystal $LiNi_{0.6}Co_{0.2}Mn_{0.2}O_2$ as high performance cathode materials for Li-ion batteries, *J. Alloys Compd.*, 2016, **674**, 360–367, DOI: 10.1016/j.jallcom.2016.03.061.

37 B. Li, Y. Wang, N. Jiang, L. An, J. Song, Y. Zuo, F. Ning, H. Shang and D. Xia, Electrolytic-anion-redox adsorption pseudocapacitance in nanosized lithium-free transition metal oxides as cathode materials for Li-ion batteries, *Nano Energy*, 2020, **72**, 104727, DOI: 10.1016/j.nanoen.2020.104727.

38 F. Zheng, C. Yang, X. Xiong, J. Xiong, R. Hu, Y. Chen and M. Liu, Nanoscale surface modification of lithium-rich layered-oxide composite cathodes for suppressing voltage fade, *Angew. Chem., Int. Ed.*, 2015, **54**, 13058–13062, DOI: 10.1002/anie.201506408.

39 S. A. Khateeb, A. G. Lind, R. Santos-Ortiz, N. D. Shepherd and K. S. Jones, Effects of steel cell components on overall capacity of pulsed laser deposited FeF_2 thin film lithium ion batteries, *J. Electrochem. Soc.*, 2015, **162**, A1667–A1674, DOI: 10.1149/2.0021509jes.

40 J. P. Perdew, K. Burke and M. Ernzerhof, Generalized gradient approximation made simple, *Phys. Rev. Lett.*, 1996, **77**, 3865–3868, DOI: 10.1103/PhysRevLett.77.3865.

41 M. D. Segall, P. J. D. Lindan, M. J. Probert, C. J. Pickard, P. J. Hasnip, S. J. Clark and M. C. Payne, First-principles simulation: ideas, illustrations and the CASTEP code, *J. Phys.: Condens. Matter*, 2002, **14**, 2717–2744, DOI: 10.1088/0953-8984/14/11/301.

42 D. Vanderbilt, Soft self-consistent pseudopotentials in a generalized eigenvalue formalism, *Phys. Rev. B: Condens. Matter Mater. Phys.*, 1990, **41**, 7892–7895, DOI: 10.1103/PhysRevB.41.7892.

43 S. P. Ong, V. L. Chevrier, G. Hautier, A. Jain, C. Moore, S. Kim, X. Ma and G. Ceder, Voltage, stability and diffusion barrier differences between sodium-ion and lithium-ion intercalation materials, *Energy Environ. Sci.*, 2011, **4**, 3680–3688, DOI: 10.1039/c1ee01782a.

44 A. I. Liechtenstein, V. I. Anisimov and J. Zaanen, Density-functional theory and strong interactions: Orbital ordering in Mott-Hubbard insulators, *Phys. Rev. B: Condens. Matter Mater. Phys.*, 1995, **52**, R5467–R5470, DOI: 10.1103/physrevb.52.r5467.

45 L. Wang, T. Maxisch and G. Ceder, Oxidation energies of transition metal oxides within the GGA+U framework, *Phys. Rev. B: Condens. Matter Mater. Phys.*, 2006, **73**, 195107, DOI: 10.1103/PhysRevB.73.195107.

46 D. H. Lee, J. Xu and Y. S. Meng, An advanced cathode for Na-ion batteries with high rate and excellent structural stability, *Phys. Chem. Chem. Phys.*, 2013, **15**, 3304–3312, DOI: 10.1039/c2cp44467d.

47 Y. Bi, M. Liu, B. Xiao, Y. Jiang, H. Lin, Z. Zhang, G. Chen, Q. Sun, H. He, F. Huang, X. Sun, D. Wang and J.-G. Zhang, Highly stable Ni-rich layered oxide cathode enabled by a thick protective layer with bio-tissue structure, *Energy Storage Materials*, 2020, **24**, 291–296, DOI: 10.1016/j.ensm.2019.08.006.

48 M. M. Thackeray, C. S. Johnson, J. T. Vaughey, N. Li and S. A. Hackney, Advances in manganese-oxide 'composite' electrodes for lithium-ion batteries, *J. Mater. Chem.*, 2005, **15**, 2257–2267, DOI: 10.1039/B417616M.

49 S. Al Khateeb, A. G. Lind, R. Santos-Ortiz, N. D. Shepherd and K. S. Jones, Cycling performance and morphological evolution of pulsed laser-deposited FeF_2 thin film cathodes for Li-ion batteries, *J. Mater. Sci.*, 2015, **50**, 5174–5182, DOI: 10.1007/s10853-015-9062-5.

50 S. Deng, X. Li, Z. Ren, W. Li, J. Luo, J. Liang, J. Liang, M. N. Banis, M. Li, Y. Zhao, X. Li, C. Wang, Y. Sun, Q. Sun, R. Li, Y. Hu, H. Huang, L. Zhang, S. Lu, J. Luo and X. Sun, Dual-functional interfaces for highly stable Ni-rich layered cathodes in sulfide all-solid-state batteries, *Energy Storage Materials*, 2020, **27**, 117–123, DOI: 10.1016/j.ensm.2020.01.009v.

51 S. Al Khateeb and T. D. Sparks, Pore-graded and conductor- and binder-free FeS_2 films deposited by spray pyrolysis for high-performance lithium-ion batteries, *J. Mater. Res.*, 2019, **34**, 2456–2471, DOI: 10.1557/jmr.2019.208.

52 S. H. Park, S. W. Oh, C. S. Yoon, S. T. Myung and Y. K. Sun, $LiN_{i0.5}Mn_{1.5}O_4$ showing reversible phase transition on 3 V region, *Electrochem. Solid-State Lett.*, 2005, **8**, A163–A167, DOI: 10.1149/1.1857113.

53 J. Zhao, Z. Wang, H. Guo and X. Li, Enhanced electrochemical properties of $LiNiO_2$-based cathode materials by nanoscale manganese carbonate treatment, *Appl. Surf. Sci.*, 2017, **403**, 426–434, DOI: 10.1016/j.apsusc.2017.01.089.

54 H. Liu, C. R. Fell, K. An, L. Cai and Y. S. Meng, In-situ neutron diffraction study of the $xLi_2MnO_3\cdot(1-x)LiMO_2$ ($x = 0, 0.5$; M = Ni, Mn, Co) layered oxide compounds during electrochemical cycling, *J. Power Sources*, 2013, **240**, 772–778, DOI: 10.1016/j.jpowsour.2013.04.149.

55 A. Gagin and I. Levin, Applications of Bayesian corrections for systematic errors in Rietveld refinements, *J. Appl. Crystallogr.*, 2016, **49**, 814–822, DOI: 10.1107/s1600576716004209.

56 Z. Ren, C. Shen, M. Liu, J. Liu, S. Zhang, G. Yang, L. Huai, X. Liu, D. Wang and H. Li, Improving $LiNi_{0.9}Co_{0.08}Mn_{0.02}O_2$'s cyclic stability via abating mechanical damages, *Energy Storage Materials*, 2020, **28**, 1–9, DOI: 10.1016/j.ensm.2020.02.028.

57 S. Liu, X. Feng, X. Wang, X. Shen, E. Hu, R. Xiao, R. Yu, H. Yang, N. Song, Z. Wang, X. Yang and L. Chen, Another strategy, detouring potential decay by fast completion of cation mixing, *Adv. Energy Mater.*, 2018, **8**, 1703092, DOI: 10.1002/aenm.201703092.

58 A. Manthiram, K. Chemelewski and E. S. Lee, A perspective on the high-voltage $LiMn_{1.5}Ni_{0.5}O_4$ spinel cathode for lithium-ion batteries, *Energy Environ. Sci.*, 2014, **7**, 1339–1350, DOI: 10.1039/c3ee42981d.

59 J. Lee, D. A. Kitchaev, D. H. Kwon, C. W. Lee, J. K. Papp, Y. S. Liu, Z. Lun, R. J. Clément, T. Shi, B. D. McCloskey, J. Guo, M. Balasubramanian and G. Ceder, Reversible Mn^{2+}/Mn^{4+} double redox in lithium-excess cathode materials, *Nature*, 2018, **556**, 185–190, DOI: 10.1038/s41586-018-0015-4.

60 S. Lee, G. Yoon, M. Jeong, M. J. Lee, K. Kang and J. Cho, Hierarchical surface atomic structure of a manganese-based spinel cathode for lithium-ion batteries, *Angew. Chem., Int. Ed.*, 2015, **54**, 1153–1158, DOI: 10.1002/anie.201408853.

61 M. D. Radin, J. Vinckeviciute, R. Seshadri and A. Van der Ven, Manganese oxidation as the origin of the anomalous capacity of Mn-containing Li-excess cathode materials, *Nat. Energy*, 2019, **4**, 639–646, DOI: 10.1038/s41560-019-0439-6.

62 R. Lin, E. Hu, M. Liu, Y. Wang, H. Cheng, J. Wu, J. C. Zheng, Q. Wu, S. Bak, X. Tong, R. Zhang, W. Yang, K. A. Persson, X. Yu, X. Q. Yang and H. L. Xin, Anomalous metal segregation in lithium-rich material provides design rules for stable cathode in lithium-ion battery, *Nat. Commun.*, 2019, **10**, 1650, DOI: 10.1038/s41467-019-09248-0.

63 J. R. Croy, K. G. Gallagher, M. Balasubramanian, Z. Chen, Y. Ren, D. Kim, S. H. Kang, D. W. Dees and M. M. Thackeray, Examining hysteresis in composite $xLi_2MnO_3\cdot(1-x)LiMO_2$ cathode structures, *J. Phys. Chem. C*, 2013, **117**, 6525–6536, DOI: 10.1021/jp312658q.

64 F. Wu, H. Lu, Y. Su, N. Li, L. Bao and S. Chen, Preparation and electrochemical performance of Li-rich layered cathode material, $Li[Ni_{0.2}Li_{0.2}Mn_{0.6}]O_2$, for lithium-ion batteries, *J. Appl. Electrochem.*, 2010, **40**, 783–789, DOI: 10.1007/s10800-009-0057-2.

65 H. Yu, Y. Wang, D. Asakura, E. Hosono, T. Zhang and H. Zhou, Electrochemical kinetics of the $0.5Li_2MnO_3\cdot0.5LiMn_{0.42}Ni_{0.42}Co_{0.16}O_2$ 'composite' layered cathode material for lithium-ion batteries, *RSC Adv.*, 2012, **2**, 8797–8807, DOI: 10.1039/c2ra20772a.

66 D. Uzun, M. Doğrusöz, M. Mazman, E. Biçer, E. Avci, T. Şener, T. C. Kaypmaz and R. Demir-Cakan, Effect of MnO_2 coating on layered $Li(Li_{0.1}Ni_{0.3}Mn_{0.5}Fe_{0.1})O_2$ cathode material for Li-ion batteries, *Solid State Ionics*, 2013, **249–250**, 171–176, DOI: 10.1016/j.ssi.2013.08.012.

67 Y. Jin, Y. Xu, X. Sun, L. Xiong and S. Mao, Electrochemically active MnO_2 coated $Li_{1.2}Ni_{0.18}Co_{0.04}Mn_{0.58}O_2$ cathode with highly improved initial coulombic efficiency, *Appl. Surf. Sci.*, 2016, **384**, 125–134, DOI: 10.1016/j.apsusc.2016.04.136.

68 H. Yu, Y. G. So, Y. Ren, T. Wu, G. Guo, R. Xiao, J. Lu, H. Li, Y. Yang, H. Zhou, R. Wang, K. Amine and Y. Ikuhara, Temperature-sensitive structure evolution of lithium–manganese-rich layered oxides for lithium-ion batteries, *J. Am. Chem. Soc.*, 2018, **140**, 15279–15289, DOI: 10.1021/jacs.8b07858.